NEW 3D CARTESIAN FLEXIBLE HINGE AND TRIPOD MECHANISM: STRESS-BASED MAXIMUM LOAD AND DISPLACEMENT WITH COMPLIANCE MODEL

NICOLAE LOBONTIU , JOZEF HUNTER, BRIAN ROBLES

Abstract. The paper develops an analytical model to assess the maximum levels of external loads and displacements of a new three-dimensional (3D) Cartesian flexible hinge and of a tripod mechanism that uses such hinges. The small-displacement compliance model is based on the allowable stresses and includes the stress concentration effect at the filleted end of the circular cross-section 3D flexible hinges. The analytical compliances of the new hinge are confirmed by finite element simulation, while the tripod piston-motion stiffness is validated by experimental testing of a prototype. The analytical model is utilized to numerically analyze the maximum loads and displacements of the new hinge and the tripod mechanism in terms of defining geometric parameters and a set of load participation factors.

Key words: Flexible, hinge, three-dimensional, Cartesian, stress, concentrator.

1. INTRODUCTION

Flexure/flexible hinges have long been implemented as elastic joints in monolithic mechanisms that are designed to perform precise, quasi-continuous, generally small-range motion in a wide spectrum of macro and micro/nano scale applications, such as positioning, manipulation, microscopy, optics, imaging systems, robotics, telecommunications, surgery or electronics, [1– 11].

While the vast majority of flexible hinges have straight centroidal axis (and are known as one-dimensional, 1D), configurations with planar, two-dimensional (2D) longitudinal axis have also been designed – see [12] for design examples from this category. Enhancing the deformation/motion capabilities of 1D and 2D flexible hinges are the three-dimensional (3D) hinge architectures, such as the Cartesian designs recently introduced and modeled in [13] and [14] and pictured in Fig. 1(a) and Fig. 1(b).

University of Alaska Anchorage, USA

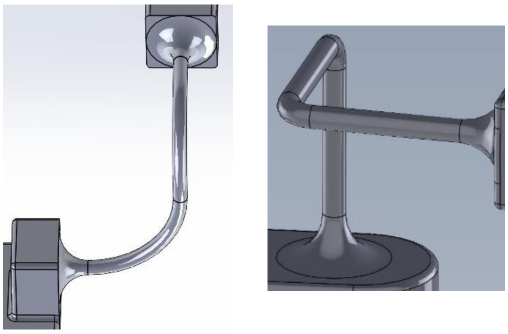

(a) (b)

Fig. 1 – 3D Cartesian right corner-filleted flexible hinges with straight-axis segments and circular-axis segments: (a) Design with two circular segments – [13]; (b) Design with two circular and three straight segments – [14].

These 3D hinges are formed of straight- and circular-axis flexible segments connected in series and located in planes that are parallel to the three planes of a right Cartesian reference frame. The hinges enable full coupling of the six degrees of freedom (DOF) at one end of the hinge with respect to the opposite end and therefore, augment the motion capabilities of 1D and 2D hinge designs.

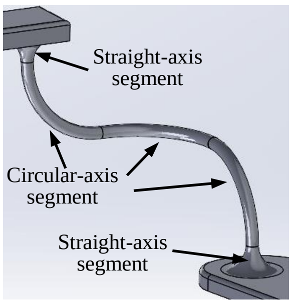

Fig. 2 – New 3D Cartesian right corner-filleted flexible hinge with three circular-axis segments.

We propose here the new 3D Cartesian flexible hinge of Fig. 2, which is formed of three circular-axis quarter-circle segments, each located in one of the three Cartesian planes. The circular-axis segments have constant circular cross-section; they are connected in series and the final hinge configuration adds two end straight-axis, right circularly corner-filleted members to mitigate stress concentration effects in the areas where the hinge connects to the adjacent (rigid) links in a mechanism. Owing to their spatial serial structure, these hinges achieve relatively large overall displacements in the linear domain, which renders them appealing in transduction applications where linear behavior is necessary.

We also study here the tripod mechanism depicted in Fig. 3, which is actually a more complex, parallel-connection hinge design formed of three identical 3D flexible hinges of the type illustrated in Fig. 2 that are connected to a moving rigid link. The tripod mechanism introduced here also displays linear force-displacement characteristic over a relatively large range and can be implemented in 3D applications, such as translation stages. Similar tripod mechanisms using 3D hinges of Fig. 1 have also been developed and characterized, as detailed in [13] and [14].

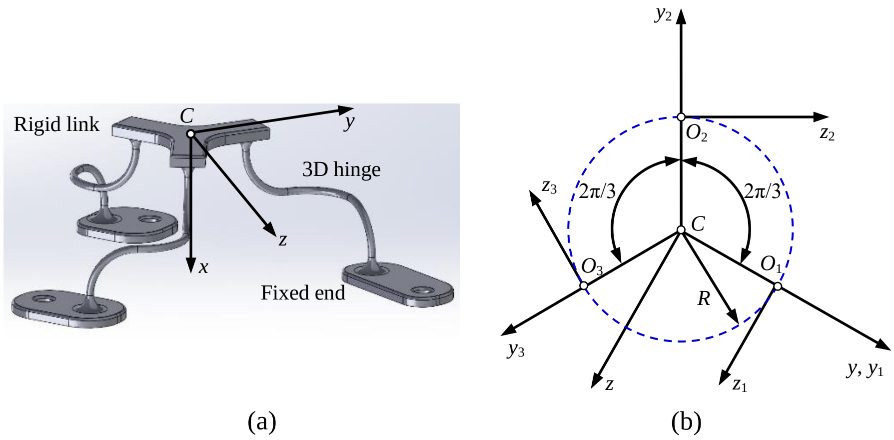

Fig. 3 – Tripod mechanism with new 3D Cartesian flexible hinges: (a) Spatial rendering with global reference frame; (b) Simplified top view with hinge reference frames.

The compliance matrix of the 3D hinge is first derived based on the small-displacement theory and existing compliances for individual segments. The analytic compliance matrix, whose components are confirmed by finite element simulation, is further utilized to formulate the compliance and stiffness matrices of the tripod mechanism. Experimental testing of a tripod prototype validated the analytical model predictions.

Stress concentration in flexible hinges and flexible-hinge mechanisms, particularly in monolithic configurations, is an important aspect that needs to be considered when evaluating the limit external loads and resulting displacements. There is a vast body of research and published literature quantifying the stress concentration of notches and shoulder fillets, see [15–22]. Flexible hinges can either be considered as notches (a straight-axis right circular hinge, for instance, is a circular or U notch) or their filleted ends can be associated with shoulder fillets.

Several straight-axis hinge configurations are studied in [23], [24] and [25] with their stress concentration factors included in the presentation.

The compliance model developed in this paper is ultimately combined with the equivalent von Mises stresses that result from bending, axial loading and torsion, as well as with the stress concentration factors at the hinge filleted end, to predict the maximum levels of external loads and resulting displacements of both the new 3D hinge and the tripod. The algorithm proposed here utilizes participation factors of the normal and shear stresses, which enables simulating a wide range of loading variants and highlighting the sensitivity of the maximum loads/displacements to geometric and topological parameters of the hinge and tripod mechanism. A similar method is presented in [12], which analyzes separately in-plane and out-of-plane stress-based loads and displacements of straight-axis flexible hinges.

2. NEW 3D FLEXIBLE HINGE

The new Cartesian 3D flexible hinge is shown as a skeleton representation (sketch) in Fig. 4(a).

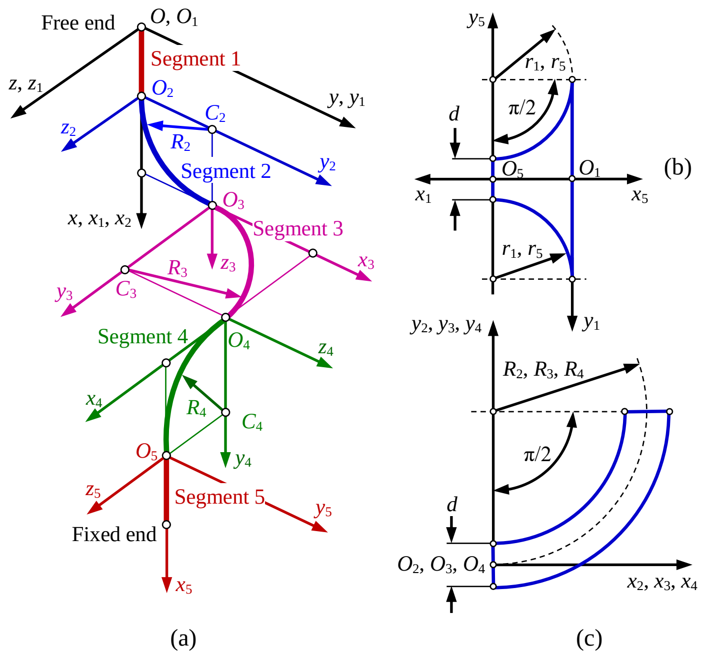

Fig. 4 – (a) Skeleton representation of the 3D Cartesian serial flexible hinge; (b) Side view of straight-axis segments; (c) Side view of circular-axis segments.

It includes two straight-axis, right circularly corner-filleted segments of radii r_1 and r_5 and – see Fig. 4(b). These two segments have variable circular cross-section of minimum diameter d, are placed at the two ends of the hinge and are aligned with global axis x. Connecting the two end segments are three circular-axis, quarter-circle segments of constant circular cross-section with diameter d and radii R_2, R_3, R_4, as illustrated in Fig. 4(c). These middle segments are the main contributors to the full hinge flexibility. Because the five component segments are located in planes parallel to one of the three global frame planes xy, yz and zx, the 3D flexible hinge is called *Cartesian* – similar configurations are analyzed in [13] and [14].

This section formulates the spatial compliance matrix of the 3D flexible hinge depicted in Fig. 4(a) based on known compliances of the five component segments. Finite element simulation is subsequently performed to confirm the analytical-model compliance predictions.

The flexible hinge of Fig. 4(a) has six DOF at its free end, which are translations u and rotations θ collected in the displacement vector $[u] = [u_x \ \ u_y \ \ \theta_z \ \ \theta_x \ \ \theta_y \ \ u_z]^T$. They are generated under the action of a spatial load vector $[f] = [f_x \ \ f_y \ \ m_z \ \ m_x \ \ m_y \ \ f_z]^T$ applied at the same point. The two vectors are related as $[u] = [C_O][f]$ where $[C_O]$ is the 3D hinge compliance matrix calculated with respect to the global frame $Oxyz$:

$$\left[C_O\right] = \sum_{i=1}^{5}\left[C_O^{(i)}\right] = \sum_{i=1}^{5}\left[T_{OO_i}\right]^T\left[R^{(i)}\right]^T\left[C_{O_i}^{(i)}\right]\left[R^{(i)}\right]\left[T_{OO_i}\right], \tag{1}$$

because of the five segments serial connection. $\left[C_{O_i}^{(i)}\right]$ (i = 1 to 5) are the local-frame compliance matrices of the straight-axis and circular-axis segments, which are explicitly provided in [13] and [14]. The five local frames are identified in Fig. 4(a). As detailed in [12], the 6 x 6 translation and rotation matrices of eq. (1) are calculated as:

$$\left[T_{OO_i}\right] = \left[f(\Delta x_i, \Delta y_i, \Delta z_i)\right]; \ \left[R^{(i)}\right] = \left[R_{\psi_i}\right]\left[R_{\theta_i}\right]\left[R_{\varphi_i}\right], \tag{2}$$

where f is a function, while Δx_i, Δy_i and Δz_i are the offsets measured along the positive global-frame directions from O to O_i. As shown in Figure 4(a), the offsets of the five local frames are: $\Delta x_1 = 0$, $\Delta x_2 = r_1$, $\Delta x_3 = \Delta x_4 = r_1 + R_2$, $\Delta x_5 = r_1 + R_2 + R_4$, $\Delta y_1 = \Delta y_2 = 0$, $\Delta y_3 = R_2$, $\Delta y_4 = \Delta y_5 = R_2 + R_3$, $\Delta z_1 = \Delta z_2 = \Delta z_3 = 0$, $\Delta z_4 = R_3$, $\Delta z_5 = R_3 + R_4$. The rotation matrix of eq. (2) is the product of three rotation matrices that express a sequence of rotations resulting in a specific local frame orientation with respect to the global frame. The rotation matrices equations can be found in [12], [13] or [14]. As per Fig. 4(a), the three rotation angles corresponding to segments 1, 2 and 5 are all zero, which means $[R^{(1)}] = [R^{(2)}] = [R^{(5)}] = [I]$, the identity matrix. The rotation angles corresponding to the other three segment frames are: $\varphi_3 = \theta_3 = \theta_4 = \psi_4 = \pi/2$, $\psi_3 = 0$, $\varphi_4 = \pi$.

Consistent with their six-DOF structure, the local-frame compliance matrices of the four segments of eq. (2) are formulated as:

$$\left[C_{O_j}^{(j)}\right]=\begin{bmatrix} C_{u_x-f_x}^{(j)} & 0 & 0 & 0 & 0 & 0 \\ 0 & C_{u_y-f_y}^{(j)} & C_{u_y-m_z}^{(j)} & 0 & 0 & 0 \\ 0 & C_{u_y-m_z}^{(j)} & C_{\theta_z-m_z}^{(j)} & 0 & 0 & 0 \\ 0 & 0 & 0 & C_{\theta_x-m_x}^{(j)} & 0 & 0 \\ 0 & 0 & 0 & 0 & C_{\theta_z-m_z}^{(j)} & -C_{u_y-m_z}^{(j)} \\ 0 & 0 & 0 & 0 & -C_{u_y-m_z}^{(j)} & C_{u_y-f_y}^{(j)} \end{bmatrix} \tag{3a}$$

$$\left[C_{O_k}^{(k)}\right]=\begin{bmatrix} C_{u_x-f_x}^{(k)} & C_{u_x-f_y}^{(k)} & C_{u_x-m_z}^{(k)} & 0 & 0 & 0 \\ C_{u_x-f_y}^{(k)} & C_{u_y-f_y}^{(k)} & C_{u_y-m_z}^{(k)} & 0 & 0 & 0 \\ C_{u_x-m_z}^{(k)} & C_{u_y-m_z}^{(k)} & C_{\theta_z-m_z}^{(k)} & 0 & 0 & 0 \\ 0 & 0 & 0 & C_{\theta_x-m_x}^{(k)} & C_{\theta_x-m_y}^{(k)} & C_{\theta_x-f_z}^{(k)} \\ 0 & 0 & 0 & C_{\theta_x-m_y}^{(k)} & C_{\theta_y-m_y}^{(k)} & C_{\theta_y-f_z}^{(k)} \\ 0 & 0 & 0 & C_{\theta_x-f_z}^{(k)} & C_{\theta_y-f_z}^{(k)} & C_{u_z-f_z}^{(k)} \end{bmatrix} \tag{3b}$$

where $j = 1$ or $j = 5$ denote the straight-axis segments 1 and 5 while $k = 2$, 3 or 4 identify the circular-axis segments 2, 3 and 4. The individual compliances of eqs. (3) are explicitly provided in [12], [13] or [14].

Four hinge designs, with their geometric parameters specified in Table 1, were used to compare the analytical and finite element (FE) compliances. Beam elements with six DOF per node were utilized in the ANSYS software to model the 3D flexible hinge of Fig. 4(a). The three circular-axis segments were meshed with 50 elements of constant cross-section while the two end straight-axis filleted segments were discretized with 10 tapered elements each. Six unit loads (three forces and three moments) were sequentially applied at the free end of the FE model and the resulting six displacements (three translations and three rotations) at the same end were queried – these displacements are the actual FE compliances. The analytical and FE values for a few compliances are included in Table 2. Both simulations employed the following material properties: Young's modulus of $97 \cdot 10^7$ N/m^2 and Poisson ratio of 0.3. The relative differences between the two methods results were very small, with maximum values not exceeding 0.5%, as also shown in Table 2.

Table 1

3D hinge designs with corresponding geometric dimensions (in [m])

Design #	d	$r_1 = r_5$	R_2	R_3	R_4
1	0.002	0.01	0.02	0.02	0.02
2	0.0015	0.01	0.03	0.02	0.03
3	0.002	0.01	0.02	0.025	0.015
4	0.002	0.015	0.02	0.02	0.02

Table 2

Analytical (A), finite element (FE) compliances and relative percentage (%) error

Design #	Results	$C_{u_y - f_y}$ [N^{-1}·m]	$C_{u_x - f_y}$ [N^{-1}·m]	$C_{u_y - m_z}$ [N^{-1}]	$C_{\theta_x - m_x}$ [N^{-1}·m^{-1}]	$C_{\theta_z - m_y}$ [N^{-1}·m^{-1}]
1	A	0.193	–0.125	–4.140	143.46	3.938
	FE	0.193	–0.125	–4.140	143.39	3.949
	% error	0	0	0	0.049	0.279
2	A	0.605	–0.393	–13.015	450.360	12.446
	FE	0.603	–0.393	–13.011	449.995	12.481
	% error	0.331	0	0.031	0.081	0.280
3	A	0.177	–0.129	–4.015	141.913	4.922
	FE	0.177	–0.129	–4.015	141.841	4.936
	% error	0	0	0	0.051	0.284
4	A	0.242	–0.146	–4.895	145.165	3.938
	FE	0.241	–0.146	–4.888	144.838	3.949
	% error	0.413	0	0.143	0.225	0.279

3. NEW TRIPOD MECHANISM

Three identical 3D flexible hinges are coupled to a rigid link, as illustrated in Fig. 3(a). Functionally, the resulting tripod mechanism is a 3D parallel-connection hinge where the input (a six-component force vector [*f*], for instance) and the output (e.g. the resulting six-component displacement vector [*u*]) are related to the common rigid link.

The three flexible hinges are connected in parallel with respect to the common rigid link; as a consequence, the tripod compliance matrix $[C_C]$ and the corresponding stiffness matrix $[K_C]$ are calculated in terms of the reference frame *Cxyz* (see Fig. 3(b)) as:

$$\left[C_C\right]=\left(\sum_{j=1}^{3}\left[C_C^{(j)}\right]^{-1}\right)^{-1}=\left(\sum_{j=1}^{3}\left[T_{CO_j}\right]^T\left[R^{(j)}\right]^T\left[C_O\right]\left[R^{(j)}\right]\left[T_{CO_j}\right]\right)^{-1} \tag{4}$$
$$\left[K_C\right]=\left[C_C\right]^{-1}.$$

The translation and rotation matrices of eq. (4) are detailed in [13] and [14]; these matrices are generically calculated as:

$$\left[T_{CO_j}\right]_{6\times 6} = \left[f(\Delta x_j, \Delta y_j, \Delta z_j)\right]; \ \left[R^{(j)}\right]_{6\times 6} = \left[R_{\psi_j}\right]\left[R_{\theta_j}\right]\left[R_{\varphi_j}\right] \tag{5}$$

The offsets of the three hinges are: $\Delta x_1 = \Delta x_2 = \Delta x_3 = 0$, $\Delta y_1 = R$, $\Delta z_1 = 0$, $\Delta y_2 = \Delta y_3 = -R\cdot\cos(\pi/3)$, $\Delta z_2 = -R\cdot\sin(\pi/3)$, $\Delta z_3 = R\cdot\sin(\pi/3)$. The rotation angles of the three hinge local frames are: $\varphi_1 = \varphi_2 = \varphi_3 = 0$, $\theta_1 = 0$, $\psi_1 = \psi_2 = \psi_3 = 0$, $\theta_2 = 2\pi/3$, $\theta_3 = 4\pi/3$. The compliance matrix $[C_O]$ of the three identical hinges is determined by means of eqs. (1), (2) and (3).

A tripod mechanism prototype was 3D printed from ABS plastic material with the following geometric parameters: $r_1 = r_5 = 0.006$ m, $R_2 = R_3 = R_4 = 0.02$ m, $d = 0.003$ m, and $R = 0.03$ m. The material Young's modulus was determined to be $E = 97\cdot 10^7$ N/m^2 and a Poisson's ratio $\mu = 0.3$ was used. The prototype and experimental setup are pictured in Fig. 5. An electromagnetic actuator (Thorlabs VC625M) was utilized to apply various forces at the tripod rigid-link center C along the vertical (x) direction and the resulting displacements along the same direction were measured by means of a laser displacement sensor (µEpsilon NCDT ILR 1320-25). Several test runs were performed, each consisting of forces increasing by a 0.5 N increment in the 1 – 6.5 N force range. The force-displacement characteristic of each test run was remarkably linear. The average experimental x-axis stiffness of the prototype tripod was 366 N/m. The corresponding analytical stiffness (calculated by means of eqs. (4) and (5)) was 371.2 N/m, which indicated an experimental-analytical relative error of 1.4%.

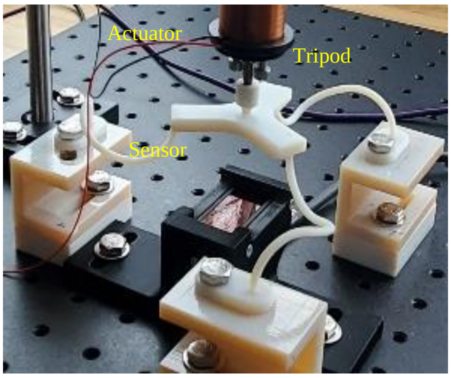

Fig. 5 – Tripod mechanism prototype with experimental setup.

4. STRESS-CONCENTRATION MAXIMUM LOAD AND DISPLACEMENTS

The maximum load and displacements are modelled here for a 3D flexible hinge, as well as for a tripod mechanism, by taking into consideration the stress concentration at the filleted root segments that are fixed.

The maximum values of the external load and resulting displacements at the free end O with respect to the other (fixed) end of the flexible hinge sketched in Fig. 4(a) are determined by the allowable levels of stresses, which are influenced by stress concentration at the filleted portion of the hinge fixed end. The flexible hinge mainly undergoes bending, torsion, and axial-load deformations under the action of the 3D load applied at O resulting in normal stresses σ and tangential (shear) stresses τ. The normal and tangential stresses are combined into an equivalent normal stress by means of von Mises criterion, which considers the state of plane stress, namely

$$\sigma_{eq} = \sqrt{\sigma^2 + 3\tau^2} \quad \rightarrow \quad \sigma_a = \sqrt{\left(K_b \sigma_{b,\max} + K_a \sigma_{a,\max}\right)^2 + 3\left(K_t \tau_{\max}\right)^2} \,. \tag{6}$$

The second eq. (6) qualifies the limit case where the stresses reach their maximum values $\sigma_{\max}$, $\tau_{\max}$ and the equivalent stress becomes the allowable normal stress σ_a. The same eq. (6) also accounts for the stress concentration factors K_b (normal bending stresses), K_a (normal axially-produced stresses) and K_t (shear, torsionally-produced stresses).

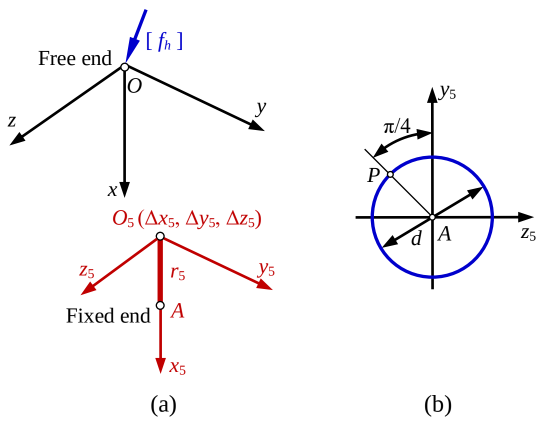

Fig. 6 – (a) Load vector [f_h] at free end of 3D Cartesian flexible hinge; (b) Net cross section at the fixed end and point P of maximum stress.

Consider the external force vector $[f_h] = [f_{hx} \;\; f_{hy} \;\; m_{hz} \;\; m_{hx} \;\; m_{hy} \;\; f_{hz}]^{\mathrm{T}}$ is applied at the free end O of a 3D Cartesian flexible hinge, as shown in Fig. 6(a) and which generates maximum loading at the fixed end A of the last segment. The corresponding maximum normal stresses result from the bending moments M_{bz} and M_{by} around the z and y axes, as well as from the axial force N. Not accounting for shear-force effects, the maximum shear stress is due to the torsion moment M_t. It can be shown that these stresses reach all a maximum at point P of Fig. 6(b). The maximum normal and shear stresses are calculated as:

$$\sigma_{\max} = \frac{M_{b,z} y_{\max}}{I} + \frac{M_{b,y} z_{\max}}{I} + \frac{N}{A}; \quad \tau_{\max} = \frac{M_t r_{\max}}{I_p}. \tag{7}$$

For the extreme case, which corresponds to maximum loads at the fixed section at end A, the maximum loads of eq. (7) are:

$$\begin{cases} M_{b,z} = -f_{hx}\left(R_2 + R_3\right) + f_{hy}\left(r_1 + R_2 + R_4 + r_5\right) + m_{hz}, \\ M_{b,y} = f_{hx}\left(R_3 + R_4\right) + m_{hy} + f_{hz}\left(r_1 + R_2 + R_4 + r_5\right), \\ M_t = f_{hy}\left(R_3 + R_4\right) + m_{hx} + f_{hx}\left(R_2 + R_3\right), \\ N = f_{hx}. \end{cases} \tag{8}$$

Given $z_{\max} = y_{\max} = \sqrt{2}d$ (see Fig. 6(b)), as well as the area properties $I = \pi d^4/64$, $I_p = \pi d^4/32$, $A = \pi d^2/4$ of the net cross section of diameter d, the maximum normal stress of eq. (7) is written as:

$$\sigma_{\max} = G_{K\sigma}(1) f_{hx} + G_{K\sigma}(2) f_{hy} + G_{K\sigma}(3) m_{hz} + G_{K\sigma}(3) m_{hy} + G_{K\sigma}(2) f_{hz}, \tag{9}$$

where the *geometric raiser factors* – introduced in [12] – that multiply the load components are:

$$\begin{aligned} G_{K\sigma}(1) &= \frac{32K_b\left(R_2 - R_4\right)}{\sqrt{2}\pi d^3} + \frac{4K_a}{\pi d^2}; \\ G_{K\sigma}(2) &= \frac{32K_b\left(r_1 + R_2 + R_4 + r_5\right)}{\sqrt{2}\pi d^3}; G_{K\sigma}(3) = \frac{32K_b}{\sqrt{2}\pi d^3}. \end{aligned} \tag{10}$$

Similarly, the maximum shear stresses are formulated as:

$$\tau_{\max} = G_{K\tau}(2) f_{hy} + G_{K\tau}(4) m_{hx} + G_{K\tau}(6) f_{hz}, \tag{11}$$

where the geometric raiser factors are:

$$G_{K\tau}(2) = \frac{16K_t\left(R_3 + R_4\right)}{\pi d^3}; G_{K\tau}(4) = \frac{16K_t}{\pi d^3}; G_{K\tau}(6) = \frac{16K_t\left(R_2 + R_3\right)}{\pi d^3} \tag{12}$$

The assumption is applied now that each of the stress terms forming $\sigma_{\max}$ in eq. (9) and $\tau_{\max}$ in Eq. (11) is a fraction c of the allowable normal stress σ_a, namely:

$$\begin{cases} G_{K\sigma}(1) f_{hx} = c_{fx}\sigma_a ;\; G_{K\sigma}(2) f_{hy} = c_{fy,\sigma}\sigma_a ; G_{K\sigma}(3) m_{hz} = c_{mz}\sigma_a ; \\ G_{K\sigma}(3) m_{hy} = c_{my}\sigma_a ; G_{K\sigma}(2) f_{hz} = c_{fz,\sigma}\sigma_a ; \\ G_{K\tau}(2) f_{hy} = c_{fy,\tau}\sigma_a ; G_{K\tau}(4) m_{hx} = c_{mx}\sigma_a ; G_{K\tau}(2) f_{hz} = c_{fz,\tau}\sigma_a . \end{cases} \tag{13}$$

Equations (13) enable expressing the maximum forces to be applied at the free end of the 3D flexible hinge:

$$\begin{cases} f_{hx,\max} = \dfrac{c_{fx}}{G_{K\sigma}(1)} \cdot \sigma_a ;\; f_{hy,\max} = \min\left(\dfrac{c_{fy,\sigma}}{G_{K\sigma}(2)} \cdot \sigma_a , \dfrac{c_{fy,\tau}}{G_{K\tau}(2)} \cdot \sigma_a \right); \\ m_{hz,\max} = \dfrac{c_{mz}}{G_{K\sigma}(3)} \cdot \sigma_a ; m_{hx,\max} = \dfrac{c_{mx}}{G_{K\tau}(4)} \cdot \sigma_a ; m_{hy,\max} = \dfrac{c_{my}}{G_{K\sigma}(3)} \cdot \sigma_a ; \\ f_{hz,\max} = \min\left(\dfrac{c_{fz,\sigma}}{G_{K\sigma}(2)} \cdot \sigma_a , \dfrac{c_{fz,\tau}}{G_{K\tau}(2)} \cdot \sigma_a \right). \end{cases} \tag{14}$$

The participation coefficients c introduced in eq. (13) are all smaller than 1. Combining eqs. (6), (7), (9) and (11) yields the following relationship between these coefficients:

$$\left(c_{fx} + c_{fy,\sigma} + c_{mz} + c_{my} + c_{fz,\sigma} \right)^2 + 3\left(c_{fy,\tau} + c_{mx} + c_{fz,\tau} \right)^2 = 1 . \tag{15}$$

The load components of eq. (14) are collected in a load vector:

$$\left[f_{h,\max} \right] = \left[f_{hx,\max} \quad f_{hy,\max} \quad m_{hz,\max} \quad m_{hx,\max} \quad m_{hy,\max} \quad f_{hz,\max} \right]^T , \tag{16}$$

that can safely be applied at the free end of the 3D flexible hinge. The maximum displacements at the same point are calculated based on the hinge compliance matrix of eq. (1) as $[u_{h,\max}] = [C_O][f_{h,\max}]$.

The individual maximum load vectors are evaluated for each of the three identical 3D flexible hinges making up the tripod mechanism in the tripod global frame based on the hinge maximum load $[f_{h,\max}]$ determined in eq. (16) as:

$$\left[f_{h,\max}^{(j)} \right] = \left[R^{(j)} \right] \left[T_{CO_j} \right] \left[f_{h,\max} \right], \quad j = 1,2,3 , \tag{17}$$

where the rotation and translation matrices of the three hinges are calculated as detailed in section 3. The maximum load applied at the center C of the tripod mechanism and the corresponding displacement vector at the same points are:

$$[f_{\max}] = \sum_{j=1}^{3}\left[f_{h,\max}^{(j)}\right]; \quad [u_{\max}] = [C_c][f_{\max}], \tag{18}$$

where the mechanism compliance matrix $[C_C]$ is expressed in eq. (4).

There are multiple ways of selecting the load participation coefficients while complying with the constraint eq. (15). We are proposing two possible choices here. One variant considers that all participation factors that are related to the normal stress have equal weights and that all coefficients derived from the shear stress have equal weights, as well:

$$c_{fx} = c_{fy,\sigma} = c_{mz} = c_{my} = c_{fz,\sigma} = c; c_{fy,\tau} = c_{mx} = c_{fz,\tau} = r_a c, \tag{19}$$

where $r_a = \tau_a/\sigma_a$ is the ratio of the allowable shear stress to the allowable normal stress. Combining eqs. (15) and (19) results in:

$$\begin{aligned} c_{fx} = c_{fy,\sigma} = c_{mz} = c_{my} = c_{fz,\sigma} = \frac{1}{\sqrt{25+27r_a^2}}; \\ c_{fy,\tau} = c_{mx} = c_{fz,\tau} = \frac{r_a}{\sqrt{25+27r_a^2}}. \end{aligned} \tag{20}$$

A typical value of the ratio r_a for most homogeneous and isotropic materials is $r_a = 0.6$.

The second variant assumes that all participation coefficients are equal except for the two coefficients connected to the force f_z; this hypothesis is consistent with the tripod mechanism operating under the sole action of the force f_z in a piston-type motion. According to this assumption:

$$c_{fx} = c_{fy,\sigma} = c_{mz} = c_{my} = c_{fy,\tau} = c_{mx} = c; c_{fz,\tau} = r_a c_{fz,\sigma}. \tag{21}$$

Eqs. (15) and (21) result in the following relationship that was derived for $r_a = 0.6$:

$$\begin{aligned} c = \frac{-(2+3r_a)c_{fz,\sigma} + \sqrt{7-3\left[(1-2r_a)c_{fz,\sigma}\right]^2}}{14} \overset{r_a=0.6}{=} \\ = 0.014\left(-19c_{fz,\sigma} + \sqrt{175-3c_{fz,\sigma}^2}\right). \end{aligned} \tag{22}$$

Because $c > 0$, a limit value resulting from eq. (22) is $c_{fz,\sigma} < 0.693$.

The approximate stress concentration factors are calculated as per [17]:

$$K_l = C_{1l} + C_{2l}\left(\frac{2r}{2r+d}\right) + C_{3l}\left(\frac{2r}{2r+d}\right)^2 + C_{4l}\left(\frac{2r}{2r+d}\right)^3, \tag{23}$$

where l stands for a (axial), b (bending) or t (torsion); the values of the coefficients C_{il} of eq. (23) for the three loading types are provided in Table 3. They are calculated based on the equations presented in Charts 3.4, 3.10 and 3.13 of [17] and on the generic circular cross-section member with shoulder fillet of Fig. 7 when considering that $t = r$ and $D = 2r + d$.

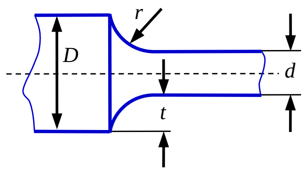

Fig. 7 – Generic member of circular cross-section with shoulder fillet – based on [17].

Table 3

Polynomial coefficients for axial, bending and torsion stress concentration factors.

	C_1	C_2	C_3	C_4
Axial	1.984	–2.063	1.931	–0.855
Bending	2.022	–2.468	2.091	–0.648
Torsion	1.613	–1.853	2.052	–0.804

The maximum loads and related displacements of the 3D flexible hinge and the tripod mechanism are influenced by the defining geometric parameters and the load participation. To identify these relationships, a numerical study has been conducted based on the analytical models developed in previous sections; a few of the resulting conclusions are formulated and included next together with some associated plots.

The six geometric stress raisers are directly influenced by the 3D hinge geometric parameters, either directly or through the stress concentration coefficients K_a, K_b and K_t as seen in eqs. (10) and (12). Increasing the values of the geometric stress raisers reduces the maximum load components, as indicated by eq. (14). Simple inspection of these equations helps formulating the following conclusions: all the geometric stress raisers increase when the diameter d decreases; increasing the fillet radii r_1 and r_5 results in larger values of $G_{K\sigma}(2)$; $G_{K\sigma}(1)$, $G_{K\sigma}(2)$ and $G_{K\tau}(6)$ increase when R_2 increases; $G_{K\tau}(2)$ and $G_{K\tau}(6)$ increase when R_3 increases; $G_{K\sigma}(2)$ and $G_{K\tau}(2)$ increase with R_4 increasing while $G_{K\sigma}(1)$ increases when R_4 decreases. Fig. 8(a) plots the variation of $G_{K\sigma}(2)$ in terms of r_5, while fig. 8(b) shows the variation of the ratio $G_{K\sigma}(2)/\, G_{K\tau}(2)$ in terms of d.

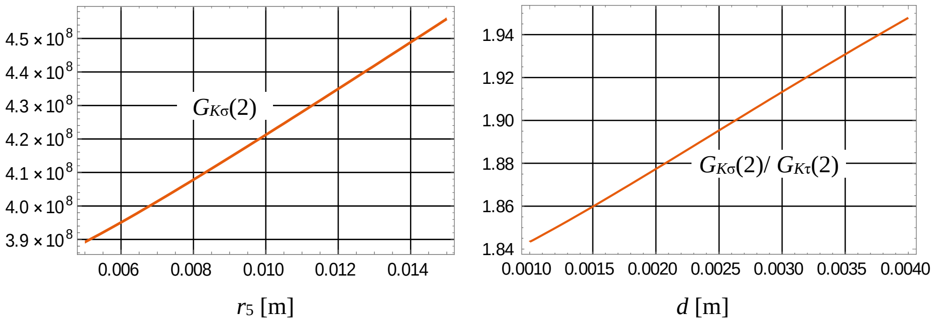

(a) (b)

Fig. 8 – Plots of geometric raisers: (a) $G_{K\sigma}(2)$ (in m^{-2}) in terms of r_5; (b) $G_{K\sigma}(2)/\ G_{K\tau}(2)$ in terms of d

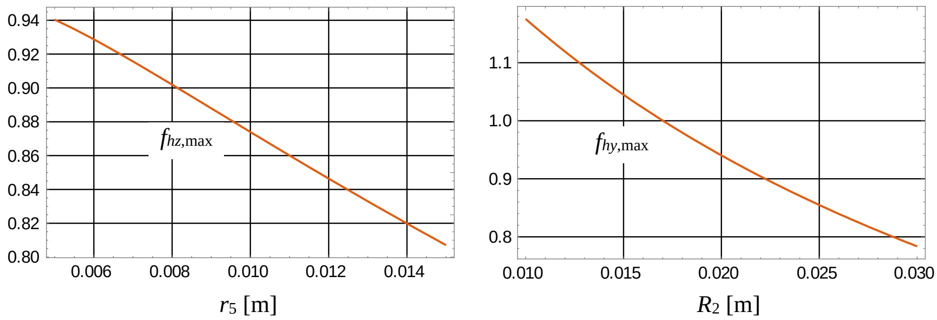

(a) (b)

Fig. 9 – Plots of hinge maximum forces (in [N]): (a) $f_{hz,\max}$ in terms of r_5; (b) $f_{hz,\max}$ in terms of R_2 .

Another set of numerical simulations analyzed the influence of geometric parameters on the maximum load to be carried by a single 3D flexible hinge. The material properties of all numerical analysis were those of stainless steel 17-4PH that is used in 3D printing of metal parts (see [26]), namely: Young's modulus E = $2{\cdot}10^{11}$ N/m^2, Poisson's ratio $\mu = 0.3$, allowable normal stress $\sigma_a = 45{\cdot}10^7$ N/m^2, and allowable stress ratio $r_a = 0.6$. The load participation coefficients were calculated as in eqs. (19) and (20) with the assumption of equal weights in normal and shear stress components. Fig. 9 illustrates the variation of two maximum hinge forces with respect to geometric parameters. Variation of all the maximum load components in terms of all the geometric parameters followed the trend described in this section in relation to the geometric stress raisers.

Fig. 10 plots the variation of the forces $f_{hz,\sigma}$ and $f_{hz,\tau}$ in terms of the load participation factor $c_{fz,\sigma}$ based on the load distribution assumption expressed in eqs. (21) and (22). It can be seen that for smaller values of $c_{fz,\sigma}$ the maximum force $f_{hz,\max}$ is $f_{hz,\sigma}$ because $f_{hz,\sigma} < f_{hz,\tau}$ – as per eq. (14) – whereas for larger values of $c_{fz,\sigma}$ the relationship between the two force components reverses and the maximum force is $f_{hz,\tau}$.

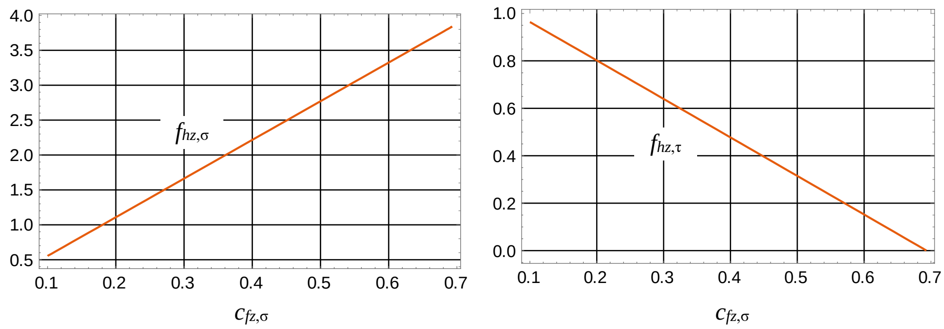

(a) (b)

Fig. 10 – Plots of hinge maximum forces (in [N]): (a) $f_{hz,\sigma}$ in terms of $c_{fz,\sigma}$; (b) $f_{hz,\tau}$ in terms of $c_{fz,\sigma}$.

The plot of Fig. 11 show the variation of the maximum hinge displacement $u_{hz,\max}$ in terms of the radius R_2. The equal-stress distribution criterion of eqs. (19) and (20) was used for these plots. Since the displacements are proportional to the external loads and the latter ones depend on the geometric stress raisers (as discussed previously in this section), the maximum hinge displacement displayed the expected variation with the geometric parameters.

Two maximum displacement $u_{z,\max}$ and maximum force $f_{z,\max}$ of the tripod rigid link center C are plotted in Fig. 12 in terms of the radius R based on equal participation in normal and shear stresses – eqs. (17), (18), (19) and (20). The other maximum loads/displacements of the tripod mechanism exhibited variations similar to those of Fig. 12.

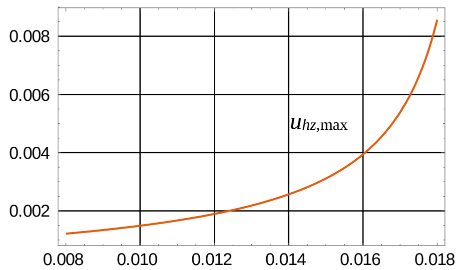

R_2 [m]

Fig. 11 – Plot of hinge maximum displacement $u_{hz,\max}$ (in [m]) in terms of R_2 .

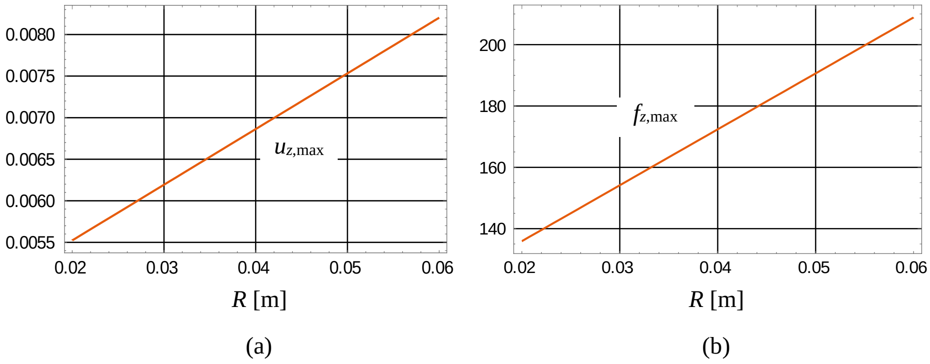

Fig. 12 – Plots of tripod performance in terms of R: (a) Maximum displacement $u_{z,\max}$ (in [m]) (b) Maximum force $f_{z,\max}$ (in [N]) .

The plots of figs. 8, 9, 10, 11 and 12 were graphed for the following constant parameters: d = 0.001 m, r_1 = 0.008 m, r_5 = 0.004 m, $R_2 = R_3 = R_4$ = 0.02 m.

Acknowledgements. The authors acknowledge the contributions of Jarod Keefe and Jason Westenskow with the experimental testing of the prototype used in this paper.

Received on December, 2021

REFERENCES

1. KYUSOJIN, A., SAGAWA, D., *Development of Linear and Rotary Movement Mechanism by Using Flexible Strips*, Bull. Jpn. Soc. Precis. Eng., **22**, *4*, pp. 309–314, 1988.
2. CHOI, Y.M. et al., *A High-Bandwidth Electromagnetic MEMS Motion Stage for Scanning Applications*, J. Micromech. Microeng., **22**, *10*, pp. 105012-1 – 9, 2012.
3. SHANG, J. et al., *A Novel Voice Coil Motor-Driven Compliant Micropositioning Stage Based on Flexure Mechanism*, Rev. Sci. Instrum., **86**, 9, pp. 095001-1 – 10, 2015.
4. CLARK, L. et al., *Design and Analysis of Compact Flexure-Based Precision Pure Rotation Stage without Actuator Redundancy*, Mech. Mach. Theory, **105**, pp. 129–144, 2016.
5. AL-JODAH, A. et al., *Modeling and a Cross-Coupling Compensation Control Methodology of a Large Range 3-DOF Micropositioner with Low Parasitic Motions*, Mech. Mach. Theory, **162**, pp. 104334-1 – 32, 2021.
6. VUKOBRATOVICH, D. et al., *Slit Diaphragm Flexures for Optomechanics*, Proc. SPIE Int. Soc. Opt. Eng., **2542**, pp. 2–10, 1995.
7. YONG, Y.K., REZA MOHEMANI, S.O., *A z-Scanner Design for High-Speed Scanning Probe Microscopy*, Proc. IEEE Int. Conf. Rob. Autom., Saint-Paul, Minnesota, USA, May 14–18, 4780, 2012.
8. REBEIZ, G.M., *RF MEMS: Theory, Design and Technology*, Wiley, New Jersey, 2003.

9. ROOPA, R., NAVIN KARANTH, P., KULKARNI, S.M., *Modeling of Compliant Flexure Diaphragm for Micropump*, Procedia Comput. Sci., **133**, pp. 1035–1039, 2018.
10. WANG, G. et al., *Design, Test and Control of a Compact Scanner Based on a Compound Compliant Amplification Mechanism*, Mech. Mach. Theory, **139**, pp. 460–475, 2019.
11. ZHANG, X., XU, Q., *Design and Development of a New 3-DOF Active-Type Constant-Force Compliant Parallel Stage*, Mech. Mach. Theory, **140**, pp. 654–665, 2019.
12. LOBONTIU, N., *Compliant Mechanisms: Design of Flexure Hinges*, Second Edition, CRC Press, Boca Raton, 2020.
13. LOBONTIU, N., WESTENSKOW, J., KEEFE, J., HUNTER, J., *New Series and Parallel 3D Cartesian Right Circularly Corner-Filleted Flexible Hinges*, Precis. Eng., **72**, pp. 653–663, 2021.
14. LOBONTIU, N., HUNTER, J., KEEFE, J., WESTENSKOW, J., *Tripod Mechanisms with Novel Spatial Cartesian Flexible Hinges*, Mech. Mach. Theory, **167**, pp. 1–16, 2022.
15. ISIDA, M., *On the Tension of the Strip with Semi-Circular Notches*, Trans. Jpn. Soc. Mech. Eng., **19**, pp. 5–10, 1953.
16. NEUBER, H., *Theory of Stress Concentration for Shear-Strained Prismatic Bodies with Arbitrary Non-Linear Stress-Strain Law*, J. Appl. Mech., **28**, pp. 545–550, 1961.
17. PILKEY, W.D., PILKEY, D.F., *Peterson's Stress Concentration Factors*, Third Edition, John Wiley & Sons, Inc., Hoboken, NJ, 2008.
18. GOMEZ, F.J. et al., *A Generalized Notch Stress Intensity Factor for U-Notched Components Loaded Under Mixed Mode*, Eng. Fract. Mech., **75**, pp. 4819–4833, 2008.
19. TAYLOR, D. et al., *The Variable-Radius Notch: Two Methods for Reducing Stress Concentration*, Eng. Fail. Anal., **18**, pp. 1009–1017, 2011.
20. ZAPPALORTO, M., BERTO, F., LAZZARIN, P., *Practical Expressions for The Notch Stress Concentration Factors of Round Bars under Torsion*, Int. J. Fatigue, **33**, pp. 382–395, 2011.
21. PANASYUK, V.V., SAVRUK, M.P., KAZBERUK, A., *Stress Concentration Near Sharp and Rounded V-Notches*, Mater. Sci., **49**, 6, pp. 711–722, 2014.
22. RADAJ, D., *State-of-the-Art Review of Extended Stress Intensity Factor Concepts*, Fatigue Fract. Eng. Mater. Struct., **37**, pp. 1–28, 2014.
23. CHEN, G., WANG, J., LIU, X., *Generalized Equations for Estimating Stress Concentration Factors of Various Notch Flexure Hinges*, ASME J. Mech. Des., **136**, pp. 031009-1 – 8, 2014.
24. ZELENIKA, S., MUNTEANU, M.GH., DE BONA, F., *Optimized Flexural Hinge Shapes for Microsystems and High-Precision Applications*, Mech. Mach. Theory, **44**, 10, pp. 1826–1839, 2009.
25. DIRKSEN, F., ANSELMANN, M., ZOHDI, T., LAMMERING, R. *Incorporation of Flexural Hinge Fatigue-Lifecycle Criteria into the Topological Design of Compliant Small-Scale Devices*, Precis. Eng., **37**, 3, pp. 531–541, 2013.
26. https://www.stratasysdirect.com, *Between the Layer Lines: Understanding 3D Printing Metal Material Nuances*.